



# Strategies for Determining the Cascade Rate in MHD Turbulence: Isotropy, Anisotropy, and Spacecraft Sampling

Yanwen Wang<sup>1</sup>, Rohit Chhiber<sup>1,2</sup> , Subash Adhikari<sup>1</sup> , Yan Yang<sup>1</sup> , Riddhi Bandyopadhyay<sup>3</sup> , Michael A. Shay<sup>1</sup> ,Sean Oughton<sup>4</sup> , William H. Matthaeus<sup>1</sup> , and Manuel E. Cuesta<sup>1</sup> <sup>1</sup> Department of Physics and Astronomy, University of Delaware, USA; [whm@udel.edu](mailto:whm@udel.edu)<sup>2</sup> Heliophysics Science Division, NASA Goddard Space Flight Center, USA<sup>3</sup> Department of Astrophysical Sciences, Princeton University, USA<sup>4</sup> Department of Mathematics, University of Waikato, Hamilton, New Zealand

Received 2022 May 11; revised 2022 August 23; accepted 2022 September 4; published 2022 September 30

## Abstract

*Exact* laws for evaluating cascade rates, tracing back to the Kolmogorov “4/5” law, have been extended to many systems of interest including magnetohydrodynamics (MHD), and compressible flows of the magnetofluid and ordinary fluid types. It is understood that implementations may be limited by the quantity of available data and by the lack of turbulence symmetry. Assessment of the accuracy and feasibility of such *third-order* (or Yaglom) relations is most effectively accomplished by examining the von Kármán–Howarth equation in increment form, a framework from which the third-order laws are derived as asymptotic approximations. Using this approach, we examine the context of third-order laws for incompressible MHD in some detail. The simplest versions rely on the assumption of isotropy and the presence of a well-defined inertial range, while related procedures generalize the same idea to arbitrary rotational symmetries. Conditions for obtaining correct and accurate values of the dissipation rate from these laws based on several sampling and fitting strategies are investigated using results from simulations. The questions we address are of particular relevance to sampling of solar wind turbulence by one or more spacecraft.

*Unified Astronomy Thesaurus concepts:* [Interplanetary turbulence \(830\)](#); [Space plasmas \(1544\)](#); [Plasma physics \(2089\)](#); [Magnetohydrodynamics \(1964\)](#); [Magnetohydrodynamical simulations \(1966\)](#)

## 1. Introduction

Direct measures of cascade rates in turbulent systems often employ theoretical formulations related to Kolmogorov’s “4/5” law (Kolmogorov 1941b; Frisch 1995) and its variants, in which the inertial range cascade rate is related to a signed third-order structure function. This so-called *exact* law is derived from the fluid equations without appeal to dimensional analysis, assumptions about scaling behavior, or any ansatz concerning timescales; however, this law does require time stationarity, spatial homogeneity, the existence of an inertial range, and a finite dissipation rate. The original formulation for isotropic incompressible hydrodynamics has been extended to magnetohydrodynamics (MHD; Politano & Pouquet 1998a, 1998b) and related models. The MHD version is frequently applied to in situ observations of plasma turbulence in the solar wind (Sorriso-Valvo et al. 2007; MacBride et al. 2008; Bandyopadhyay et al. 2020) to obtain cascade rates that inform theories of heating and acceleration of the solar wind (Osman et al. 2011), providing ground truth for related approximations in space physics (Vasquez et al. 2007). Frequently a major issue in these applications is the use of formulations derived assuming isotropy in turbulence that is actually anisotropic (Verdini et al. 2015), this being the typical case for solar wind and magnetosheath turbulence. Usually this potential inconsistency is disregarded in favor of extensive averaging, whenever possible. Another more practical limitation is the challenging requirement of a sufficient volume of data (Podesta

et al. 2009), a kinematic and statistical issue further complicated by potential sensitivity to the tails of the probability distribution of the fluctuations (Dudok de Wit 2004). Taking these challenges into account, we note that the ability to extract cascade rates from observational data is of increasing importance due to the centrality of fundamental questions relating to heating and dissipation in space and astrophysical plasmas (e.g., Kiyani et al. 2015). Therefore, in the present study we revisit several related issues that are pertinent to the evaluation of third-order laws using single-point or multi-point measurements. We reexamine the issue of averaging by focusing on conditions for obtaining accurate results in both isotropic and anisotropic turbulence. The strategies we examine are implemented using data from three-dimensional (3D) MHD turbulence simulations. A motivation for this approach is that for such cases we have an unambiguous determination of the underlying turbulence symmetry as well as a straightforward method to quantify the absolute dissipation rate.

The remainder of the paper is structured as follows. In Section 2, we review relevant theoretical and observational studies that set the stage for the questions we address. Section 3 describes in detail the simulations used for the present study. Section 4 contains the results for the one-dimensional (1D) form of the third-order law using measurements for the isotropic and anisotropic cases. Section 5 delves into the direction-averaged 1D form of the third-order law in the inertial range and shows the effect of all terms in the von Kármán–Howarth equation. Section 6 provides an example of using the 1D form third-order law in a single spacecraft sample, and discusses the relative accuracy of this strategy to estimate the energy dissipation rate in observational measurements.



Original content from this work may be used under the terms of the [Creative Commons Attribution 4.0 licence](#). Any further distribution of this work must maintain attribution to the author(s) and the title of the work, journal citation and DOI.

Section 7 provides a summary of the results, and examines the relationship between the strategies used in this study and their potential applications to multipoint observations via a constellation of spacecraft.

## 2. Background

### 2.1. Theory

We start from the 3D incompressible MHD equations (e.g., Biskamp 2003)

$$\begin{aligned} \frac{\partial \mathbf{v}}{\partial t} + \mathbf{v} \cdot \nabla \mathbf{v} &= -\nabla P + \mathbf{B} \cdot \nabla \mathbf{B} + \nu \nabla^2 \mathbf{v}, \\ \frac{\partial \mathbf{B}}{\partial t} + \mathbf{v} \cdot \nabla \mathbf{B} &= \mathbf{B} \cdot \nabla \mathbf{v} + \mu \nabla^2 \mathbf{B}, \end{aligned} \quad (1)$$

where  $\mathbf{v}$  and  $\mathbf{B}$  represent the local velocity and magnetic field (the latter in Alfvén speed units with  $\mathbf{B}/\sqrt{4\pi\rho} \rightarrow \mathbf{B}$  and uniform mass density  $\rho$ ),  $P$  is the total (thermal plus magnetic) pressure,  $\nu$  is the kinematic viscosity, and  $\mu$  is the resistivity. Note that  $\mathbf{B} = \mathbf{B}_0 + \mathbf{b}$  where  $\mathbf{B}_0$  is the global mean field and  $\mathbf{b}$  is the fluctuating field. As is well known, one may work with the Elsässer variables (Elsässer 1950),  $\mathbf{z}^\pm(\mathbf{r}) = \mathbf{v}(\mathbf{r}) \pm \mathbf{b}(\mathbf{r})$ , instead of  $\mathbf{v}$  and  $\mathbf{b}$ . For situations where  $\nu = \mu$ , the incompressible MHD equations are then rewritten as

$$\begin{aligned} \frac{\partial}{\partial t} \mathbf{z}^\pm &= -(\mathbf{z}^\mp \cdot \nabla) \mathbf{z}^\pm \\ &\quad - \nabla P + \nu \nabla^2 \mathbf{z}^\pm \pm (\mathbf{B}_0 \cdot \nabla) \mathbf{z}^\pm. \end{aligned} \quad (2)$$

By taking the difference between the equation at  $\mathbf{z}^\pm(\mathbf{r})$  and that at  $\mathbf{z}^\pm(\mathbf{r} + \ell)$ , and assuming homogeneity and incompressibility, the pressure term and the term containing  $\mathbf{B}_0$  vanish. Let us define

$$\delta \mathbf{z}^\pm(\mathbf{r}, \ell) = \mathbf{z}^\pm(\mathbf{r} + \ell) - \mathbf{z}^\pm(\mathbf{r}) \quad (3)$$

as the *increment* of the Elsässer variables. Taking now the dot product of  $\delta \mathbf{z}^\pm$  with the equation for  $\partial(\delta \mathbf{z}^\pm)/\partial t$  and performing an ensemble average of the result yields the MHD von Kármán–Howarth equation (Politano & Pouquet 1998a, 1998b):

$$\frac{\partial}{\partial t} \langle (\delta \mathbf{z}^\pm)^2 \rangle = -\nabla_\ell \cdot \langle \delta \mathbf{z}^\mp | \delta \mathbf{z}^\pm |^2 \rangle + 2\nu \nabla_\ell^2 \langle (\delta \mathbf{z}^\pm)^2 \rangle - 4\epsilon^\pm. \quad (4)$$

Recall that because of homogeneity taking either an ensemble average (McComb 1990) or a spatial average (denoted as  $\langle \bullet \rangle$ ), means that the averaged increments  $\langle \delta \mathbf{z}^\pm(\mathbf{r}, \ell) \rangle$  are only dependent on the lag  $\ell$ , and similarly for other moments of the increments. Here,  $\epsilon^\pm = \nu \langle [|\nabla \mathbf{z}^\pm(\mathbf{r})|^2] \rangle$  are the mean dissipation rates associated with the Elsässer energies  $\langle \mathbf{z}^\pm \cdot \mathbf{z}^\pm \rangle / 2$  (not the increments). Since these dissipation rates involve real-space gradients (i.e.,  $\nabla$  not  $\nabla_\ell$ ) and are independent of lag, they are constant over all length scales. The total energy dissipation rate of the system, also lag independent, is

$$\epsilon_{\text{diss}} = \frac{\epsilon^+ + \epsilon^-}{2} = \nu \langle \omega^2 + J^2 \rangle, \quad (5)$$

where the second form is in terms of the mean-square vorticity  $\langle \omega^2 \rangle = \langle (\nabla \times \mathbf{v})^2 \rangle$  and mean-square electric current density  $\langle J^2 \rangle = \langle (\nabla \times \mathbf{b})^2 \rangle$ .

Equation (4) is the fundamental equation of energy conservation on which all related results presented below will be based. The terms of Equation (4) express four effects: time dependence, nonlinear transfer, dissipation (of the mean-square increments), and the exact dissipation rate of Elsässer energies, respectively, from left to right. For convenience in referring to the first three of these terms, which are lag dependent, we designate  $\frac{\partial}{\partial t} \langle (\delta \mathbf{z}^\pm)^2 \rangle = T^\pm$ ,  $\langle (\delta \mathbf{z}^\pm)^2 \rangle = G^\pm$ , and

$$\mathbf{Y}^\pm(\ell) = \langle \delta \mathbf{z}^\mp | \delta \mathbf{z}^\pm |^2 \rangle. \quad (6)$$

The quantities  $\mathbf{Y}^\pm$ , the *Yaglom fluxes*, are the only *third-order* structure functions present. The MHD von Kármán–Howarth equation, Equation (4), can then be rewritten as

$$T^\pm + \nabla_\ell \cdot \mathbf{Y}^\pm - 2\nu \nabla_\ell^2 G^\pm = -4\epsilon^\pm. \quad (7)$$

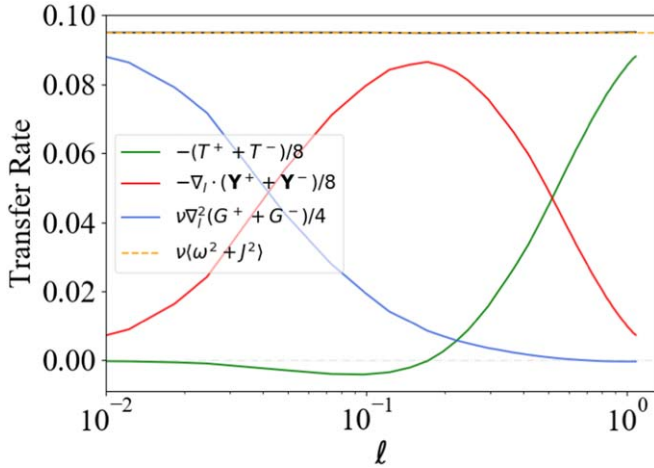
We will also make use of the sum of these equations which represents scale-by-scale conservation of the total (flow plus magnetic) energy rather than that of the Elsässer energies. Writing  $T = T^+ + T^-$ , and similarly for  $Y$  and  $G$ , we have

$$T + \nabla_\ell \cdot \mathbf{Y} - 2\nu \nabla_\ell^2 G = -8\epsilon_{\text{diss}}. \quad (8)$$

Below we will refer to the  $\nabla_\ell \cdot \mathbf{Y}^\pm$  terms as the Yaglom term, recalling that it represents nonlinear transfer of energy across scales. In this scale-by-scale energy balance equation,  $T$  represents the time rate of change of energy at scales smaller than  $\ell$ , while the term involving  $G$  is the dissipation at scales larger than  $\ell$ .

Much of the remainder of this paper will examine various approximations and idealizations in which important information, especially the dissipation rates  $\epsilon^\pm$  and  $\epsilon_{\text{diss}}$ , can be extracted easily, and to varying extents, accurately from Equations (7) and (8). We emphasize the following properties of this central equation: (i) It is exact, subject to the assumptions of spatial homogeneity and incompressibility; (ii) It depends on the 3D structure functions of the various terms in vector lag ( $\ell$ ) space; (iii) It does not require very large Reynolds numbers; and (iv) It is much more general than the various forms of third-order laws (Politano & Pouquet 1998a, 1998b) that are commonly implemented to estimate  $\epsilon_{\text{diss}}$ .

The governing Equation (7) is rather versatile as a starting point for determining the bookkeeping of energy at all scales, including its supply from large scales, its transfer across scales and its dissipation into heat. When appropriate the transfer across scales will be considered to be a *cascade* as will be discussed more precisely below. Equation (7) holds at *every* point in 3D lag space, so if the terms involving  $T^\pm$ ,  $\mathbf{Y}^\pm$ , and  $G^\pm$  are known at any point, then  $\epsilon_{\text{diss}}$  can be determined. However, this requires accurate determination of first and second derivatives in multiple independent lag directions, in general. Such information is formally available in high-resolution 3D simulations, but since such derivatives will be evaluated approximately, averaging results over different  $\ell$ 's—usually at constant  $\ell = |\ell|$ —is useful to achieve accuracy. To set the stage for subsequent results we begin with an illustrative example of this type, based on one of our simulations (discussed fully in the following section). We note that related recent studies have also implemented a direct evaluation of terms in the MHD von Kármán–Howarth equations, including direction averaging (Hellinger et al. 2018; Adhikari et al. 2021; Yang et al. 2022).



**Figure 1.** Terms of the von Kármán–Howarth equation, Equation (7), evaluated using the anisotropic ( $\mathbf{B}_0 = 2\hat{z}$ ) simulation III at  $t = 3.2$ . Here,  $\frac{\partial}{\partial t} \langle (\delta z^\pm)^2 \rangle = T^\pm$ ,  $\langle \delta z^\mp | \delta z^\pm|^2 \rangle = Y^\pm$ , and  $\langle (\delta z^\pm)^2 \rangle = G^\pm$ . The green, red, and blue curves correspond to the three left-hand side (LHS) terms in Equation (8), averaged over many directions of vector lag  $\ell$ . Lag is expressed in units of the simulation box length ( $2\pi$ ). The orange horizontal dashed line indicates the exact dissipation rate  $\epsilon_{\text{diss}} = \nu(\omega^2 + J^2)$ . The black curve is the sum of the three (LHS) terms: the large-scale energy supply, the nonlinear transfer rate to smaller scales, and the dissipation at scales larger than  $\ell$ . As expected, they add up to the total dissipation rate.

Shown in Figure 1 are the (direction-averaged) terms of the von Kármán–Howarth equation, Equation (7), plotted versus the magnitude of the lag for a selected incompressible MHD simulation. Upon averaging over directions, the terms in Figure 1 only depend on lag length  $\ell$ . It is readily seen that the (appropriate combinations of the)  $T^\pm$ ,  $Y^\pm$ , and  $G^\pm$  terms quite precisely sum to the value of  $\epsilon_{\text{diss}}$ . This represents the exact conservation of energy; specifically, for any chosen length scale, the sum of the rates of change of energy due to all processes is zero.

It is also apparent that the different terms  $T^\pm$ ,  $Y^\pm$ , and  $G^\pm$  in Equation (7) make their principle contribution in different ranges of scales. In this particular simulation, such *separation of scales* is not perfect; this is discussed further below. This points to the most commonly encountered simplification of scale-dependent energy balance, namely, the possibility of an *inertial range*. In the original hydrodynamic context, Kolmogorov (1941a) postulated that an inertial range is obtained asymptotically at an infinite Reynolds number.

The onset of an inertial range is expected when the large energy-containing eddies become well separated from the scales at which dissipation occurs. This has been shown in some detail in high Reynolds number hydrodynamics experiments (e.g., Antonia & Burattini 2006). For a true inertial range, the Yaglom term  $-\nabla_\ell \cdot \mathbf{Y}^\pm/4$  is the only significant contribution to Equation (7) over this range of lag  $\ell$  (i.e., this term is  $\gg$  the other terms) and we say that the Yaglom term determines the *cascade rate*. Ideally the contribution of the Yaglom term is flat over a span of lags. Figure 1 exhibits only a hint of the emergence of such a clear scale separation and therefore the phrase *inertial range* is only loosely applicable for that simulation. Note, however, that the presence or absence of an inertial range does not influence the accuracy of Equation (7) in any way.

### 2.1.1. Third-order (aka Yaglom) Laws

In a well-established (i.e., large bandwidth) inertial range, both the time variation term ( $-T^\pm/4$ ) and the scale-dependent dissipation term ( $\nu \nabla_\ell^2 G^\pm/2$ ) are small. If these terms become vanishingly small over an intermediate scale range then—without assuming isotropy—one obtains the simplified equation:

$$\nabla_\ell \cdot \mathbf{Y}^\pm = \nabla_\ell \cdot \langle \delta z^\mp | \delta z^\pm|^2 \rangle = -4\epsilon^\pm. \quad (9)$$

Such two-term specializations of the von Kármán–Howarth equation are called *third-order* or *Yaglom laws*. Herein we refer to Equation (9) as the *divergence form*, or 3D form, of the MHD third-order law. A point of emphasis is that to obtain these forms requires that the Reynolds number is large enough that an effectively dissipation-free (inertial) range exists, and that the energy content of this range is steady. These assumptions are in addition to the requirements of homogeneity and incompressibility that are inherited from the developments leading to Equation (7). Isotropy is not required.

*Isotropy.* An important historical development was the imposition of isotropy on Equation (9), which leads to its further simplification. This was originally done for hydrodynamics (Kolmogorov 1941b) and later for MHD (Politano & Pouquet 1998a, 1998b). Assuming then that the MHD turbulence is isotropic, Equation (9) may be directly integrated to provide a 1D form, or the isotropic form, for the third-order law (Politano & Pouquet 1998b; Osman et al. 2011):

$$Y_\ell^\pm = \langle (\hat{\ell} \cdot \delta z^\mp) | \delta z^\pm|^2 \rangle = -\frac{4}{3}\epsilon^\pm \ell, \quad (10)$$

sometimes called a 4/3 law. There are also equivalent forms that use just the longitudinal increments—sometimes called the 4/5 laws (Kolmogorov 1941b; Frisch 1995; Politano & Pouquet 1998a).

*Direction averaging.* Although isotropy can be established a priori only rarely, the isotropic or 1D form of the third-order law is nonetheless still often used in observational or experimental situations (Sorriso-Valvo et al. 2007; MacBride et al. 2008). The utility of this approach may be understood better when the technique is supplemented by direction averaging, carried out in an appropriate way. This very important and intuitively appealing idea has been developed in the hydrodynamics literature (Nie & Tanveer 1999; Taylor et al. 2003). The analogous result for incompressible MHD follows by direct extension of the hydrodynamic case. Below we present an abbreviated version of this straightforward derivation for MHD.

We proceed by direction averaging the fundamental energy balance relation, Equation (7). Carrying out a full integration over all directions,<sup>5</sup> and using an overbar to designate averaging over the full  $4\pi$  solid angle, e.g.,  $\overline{\nabla_\ell \cdot \mathbf{Y}^\pm} = (4\pi)^{-1} \int_S \nabla_\ell \cdot \mathbf{Y}^\pm d\Omega = (4\pi)^{-1} \int_0^\pi \int_0^{2\pi} \nabla_\ell \cdot \mathbf{Y}^\pm \sin\theta d\phi d\theta$ , we find, without loss of generality, that

$$\overline{T^\pm} + \overline{\nabla_\ell \cdot \mathbf{Y}^\pm} - 2\nu \overline{\nabla_\ell^2 G^\pm} = -4\epsilon^\pm. \quad (11)$$

It is readily shown that the angular parts of the  $\nabla_\ell$  operators do not contribute when the averaging is taken into account. Some details are provided in Appendix. The direction-averaged von

<sup>5</sup> Using spherical polar coordinates.



Kármán–Howarth equation becomes

$$\overline{T^\pm} + \frac{1}{\ell^2} \frac{d}{d\ell} [\ell^2 \overline{Y_\ell^\pm}] - \frac{2\nu}{\ell^2} \frac{d}{d\ell} \left[ \ell^2 \frac{d}{d\ell} \overline{G^\pm} \right] = -4\epsilon^\pm$$

or,

$$\overline{T^\pm} + \mathcal{D}_\ell^{(1)} \overline{Y_\ell^\pm} - 2\nu \mathcal{D}_\ell^{(2)} \overline{G^\pm} = -4\epsilon^\pm, \quad (12)$$

where each term on the LHS depends on the scalar lag  $\ell = |\ell|$ . In Equation (12), for convenience of the presentation later, we have introduced the shorthand notation  $\mathcal{D}_\ell^{(1)} \equiv \frac{1}{\ell^2} \frac{d}{d\ell} [\ell^2 *]$  for the radial contribution to the divergence operator, and the radial part of the Laplacian operator, with dummy arguments  $*$ , and both defined in the lag space. We emphasize this explicitly to distinguish the form of Equation (7), which involves 3D vector operations, while Equation (12) involves only the reduced dimensional 1D operations.

This direction-averaged form of the von Kármán–Howarth equation, Equation (12), remains quite general requiring only spatial homogeneity and incompressibility. If the system is also time stationary, or if suitable time averaging is performed (Taylor et al. 2003), the first term,  $\overline{T^\pm}$ , may be safely neglected. Following the usual arguments, when the Reynolds number is sufficiently large ( $\nu$  sufficiently small), the dissipative term involving  $\overline{G^\pm}$  is also negligible over an intermediate range, which becomes the inertial range. In that case, the remaining ordinary differential equation is

$$\mathcal{D}_\ell^{(1)} \overline{Y_\ell^\pm} = \frac{1}{\ell^2} \frac{d}{d\ell} [\ell^2 \overline{Y_\ell^\pm}] = -4\epsilon^\pm, \quad (13)$$

which immediately integrates into the *direction-averaged third-order law* (see Equation (A6) in the Appendix)

$$\overline{Y_\ell^\pm} = -\frac{4}{3} \epsilon^\pm \ell. \quad (14)$$

Although this is structurally identical to the 1D form third-order law associated with an inertial range in *isotropic* cases, Equation (10), we emphasize that there are several important distinctions between Equations (10) and (14). The former holds at any (inertial range) vector lag  $\ell$  but only for isotropic turbulence. The latter holds for *any* rotational symmetry (or lack thereof) but requires averaging (the full  $4\pi$ ) solid angle.

The third-order (Yaglom) laws for hydrodynamics and MHD should be applied in situations in which one may reasonably assume that the conditions leading to these relations are actually attained. However, in general the most frequently quoted conditions—time stationarity, homogeneity in space, and high Reynolds numbers—may not always hold and a pristine inertial range may not appear. In such cases, the range over which a third-order law might be applied may be *polluted* by other terms in Equation (7).

The exact statement of energy conservation in Equation (4) or (7) provides a complete specification of the energy balance in homogeneous turbulence when evaluated over arbitrary regions of the (vector) lag space. When the full energy balance cannot be computed, it is common practice to resort (sometimes without demonstrating justification) to more compact third-order laws—such as Equations (9), (10), and (14)—all of which require that the time-dependent terms  $T^\pm$  and dissipative terms  $G^\pm$  are negligible for a useful region of lag space.

Below we provide several examples of different approaches to approximately measure the inertial range transfer rate

(sometimes loosely called the *cascade rate*) using MHD simulation data:

*Method I.* The unidirectional 1D form, Equation (10), is evaluated for a fixed lag direction, over a range of lag magnitudes. This is suitable for isotropic systems. The choice of direction is clearly not unique but should not matter for a truly isotropic system. There are several variations: Equation (10) can be evaluated over a range of lags with a linear fit (through the origin) giving  $\epsilon^\pm$ . Alternatively, the equation can first be divided by  $\ell$  and the result plotted, allowing estimation of  $\epsilon^\pm$  from a suitable flat range.

*Method II.* The 3D (or divergence) form, Equation (9), can be used to compute  $\epsilon^\pm$  when 3D lag-space derivatives can be reliably determined in several directions. This method is based on a direct evaluation of (derivatives of) the  $Y^\pm$  terms in the von Kármán–Howarth Equation (7) and is fully general in terms of turbulence symmetries when inertial range conditions are obtained. No direction averaging is required although averaging may reduce statistical inaccuracies. In this paper, the only occasion where the 3D lag-space derivatives are calculated is when obtaining the curves shown in Figure 1.

*Method III.* The direction-averaged 1D form, Equation (14), is exact when integrated over the full spherical domain of lags, provided that inertial range conditions are established. However, a full integration over direction may not be feasible with available measurements. In practice, a discretized approximation to the continuum average is likely to be needed. This may be obtained, for example, by calculating  $Y_\ell^\pm$  for each of the (limited number of) available directions of  $\ell$  and then forming the appropriately weighted average of these, see, for example, Equation (A7).

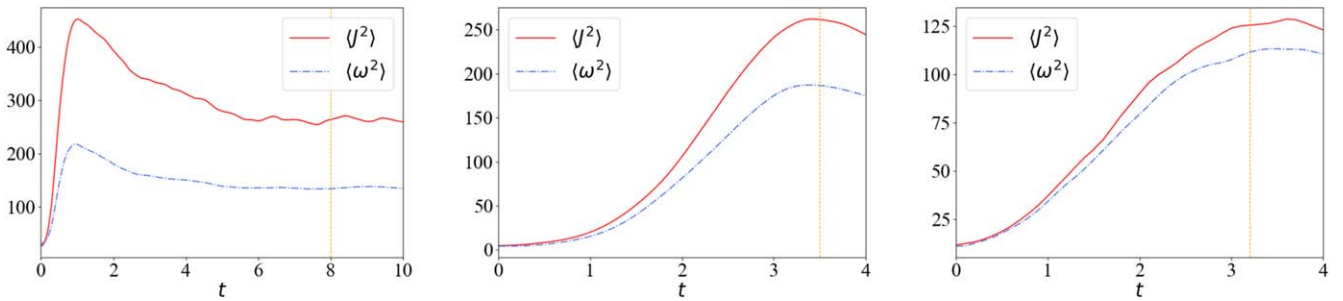
All three of the above methods, being based on third-order laws, require the existence of an inertial range, at least approximately. Otherwise, and more generally, when the  $T^\pm$  and  $G^\pm$  terms are significant, it is appropriate to use more complete forms of the von Kármán–Howarth equation, such as Equation (7) or (12).

## 2.2. Observational Approaches and Limitations

Typical solar wind studies of turbulence are carried out with single spacecraft measurements and in a high-speed flow for which time correlations can be interpreted as spatial correlations with reasonable accuracy (Jokipii 1971). In these circumstances, observational analyses typically compute a cascade rate by employing 1D forms of the third-order law or its generalizations. In space plasma measurements, it is difficult to obtain the time variation and the dissipative terms in the von Kármán–Howarth equation Equation (4) or (7), and therefore only the  $\nabla_\ell \cdot Y^\pm$  terms (or really their integrals) can be calculated using in situ data from single spacecraft.

Most frequently Method I, Equation (10), is employed for cascade rate estimation in the solar wind (MacBride et al. 2005; Sorriso-Valvo et al. 2007; MacBride et al. 2008). Implicit in this approach is the assumption of isotropy, although the accuracy of this approximation has rarely been demonstrated. There have been attempts to adapt the 1D forms in order to refine the method (Stawarz et al. 2009; Coburn et al. 2015) by making various assumptions about the structure and symmetry of the Yaglom flux.

The 1D forms, essentially Equation (10), have also been applied in the Earth’s magnetosheath (Bandyopadhyay et al. 2020) and in Parker Solar Probe (PSP) data near perihelia



**Figure 2.** Time evolution of  $\langle J^2 \rangle$  and  $\langle \omega^2 \rangle$  for Runs I (left), II (middle), and III (right). The vertical orange line indicates the time for performing the analysis.

**Table 1**  
Simulation Parameters

Run	Type	Symmetry	Resolution (3D)	$B_0$	$\delta b/B_0$	$k$ Range	$\nu = \mu$	$\sigma_c$	$\epsilon_{\text{diss}}$	$\ell_{\text{diss}} = (\nu^3/\epsilon_{\text{diss}})^{1/4}$
I	Driven	Isotropic	512	0	...	3-5	$2.0 \times 10^{-3}$	-0.05	0.795	0.010
II	Decaying	Anisotropic	1024	1	1	1-3	$4.0 \times 10^{-4}$	0.09	0.179	0.0043
III	Decaying	Anisotropic	1024	2	0.5	1-5	$4.0 \times 10^{-4}$	0.7	0.0948	0.0051

**Note.** The global magnetic field  $\mathbf{B}_0$  is in the  $\hat{z}$  direction. The rms magnetic fluctuation is  $\delta b = \sqrt{\langle b^2 \rangle}$ , and  $\delta b/B_0$  measures the initial relative strength of the fluctuations. Column “ $k$  Range” indicates the wavenumber forcing band (Run I) or the initial conditions band (Runs II and III). Viscosity  $\nu$  equals resistivity  $\mu$  for each simulation. The normalized cross helicity  $\sigma_c$ , energy dissipation rate  $\epsilon_{\text{diss}}$ , and dissipation scale  $\ell_{\text{diss}}$  are computed at the respective times of analysis indicated in Figure 2.

(Bandyopadhyay et al. 2020) where turbulence is much more intense than at 1 au. It is noteworthy that there is considerable recognition that averaging is required, although this typically takes the form of a requirement for large data volumes and large data sets (Dudok de Wit 2004; Podesta et al. 2009) rather than a requirement for averaging over lag directions.

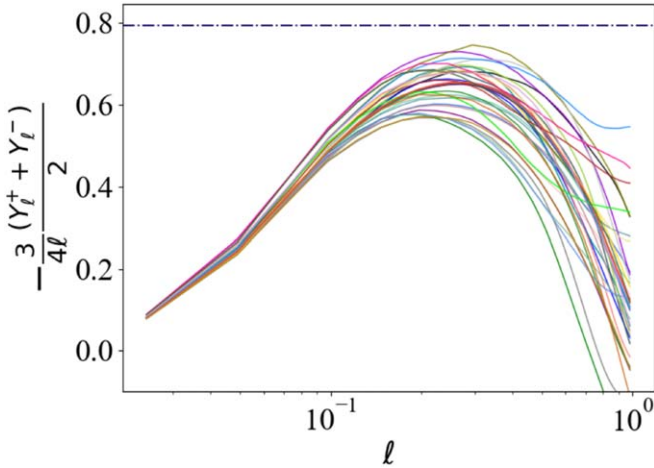
In single spacecraft measurements (with the Taylor hypothesis) it is feasible to improve accuracy by averaging several measurements (MacBride et al. 2008). However, this averaging method is still not considered as the 3D form Equation (9), and generally the weighting of different directions has not been considered. In particular, keeping in mind the results summarized in the previous section, finite sampling strategies generally do not guarantee a uniform distribution of lag directions on a sphere. In this regard, a very important development is the recognition that the Yaglom flux varies systematically over the direction relative to the mean magnetic field (Verdini et al. 2015). However the assembly of measurements into a proper averaging over the unit sphere—essentially the result obtained by Nie & Tanveer (1999) in hydrodynamics extended to the MHD third-order law (Politano & Pouquet 1998a) as in Equation (14)—has apparently not been fully appreciated in previous MHD and space physics studies. There has been at least one study (Osman et al. 2011) employing multi-spacecraft Cluster data that accumulated the normal flux over a sphere in lag space, approximately carrying out the operations implied by Method III, Equation (14). Such data sets are infrequently available in the solar wind.

As a consequence, it is crucial to know how accurately one might estimate the cascade or dissipation rate when computed from Method I, the 1D form Equation (10), in various situations. This may be challenging in the solar wind, where the existence of a strong global magnetic field implies significant anisotropy. Proper direction averaging may not always be possible, unless very large ensembles are considered, as in, for example, recent ensemble average computations of correlation function that employed years of data and proper

normalization of individual samples (Roy et al. 2021). However the intent of cascade rate estimation is often to understand more *local* conditions, so the emphasis may be on very much more local averaging. Such cases are severely constrained by the availability of single spacecraft data and the number of directions relative to the mean magnetic field that can be sampled. For an examination of the distribution of flow-magnetic field directions at 1 au, see the analysis of this question based on the MMS Turbulence Campaign in the solar wind by Chasapis et al. (2020). The remainder of this paper is largely devoted to exploring the accuracy of energy transfer (cascade) rate measurements using von Kármán–Howarth equations and third-order laws in various forms.

### 3. Simulations

In order to study the energy cascade rate in MHD turbulence using third-order structure functions, we analyze data from several incompressible 3D MHD turbulence simulations. Key parameters of the simulations employed are shown in Table 1. For all simulations in the table, the domain is a three-dimensional periodic box with sides of length  $2\pi$ , and the MHD equations are solved using a Galerkin spectral method (Orszag & Patterson 1972; Oughton & Matthaeus 2020). Each simulation is initialized with the condition that the fluctuation magnetic energy and fluid flow energy are equal, such that  $E_m = E_f = 0.5$ . Also, the viscous and resistive dissipation coefficients,  $\nu$  and  $\mu$ , are set equal. These parameters act, respectively, as the reciprocal Reynolds number and the magnetic Reynolds number. The normalized cross helicity,  $\sigma_c = \langle \mathbf{v} \cdot \mathbf{b} \rangle / (E_f + E_m)$ , is known to be a significant factor in the evolution of turbulent MHD (Pouquet et al. 1986). Run III has a substantial value of  $\sigma_c$ , and this case will be qualitatively contrasted with the lower cross helicity case in run II. A full scan of parameters such as  $\sigma_c$  will not be attempted in this study. Runs II and III are undriven and anisotropic, with distinct values of  $B_0$ . Run I is isotropic and driven; this case is



**Figure 3.** Estimating the dissipation rate using Method I, the 1D form third-order law (Equation (10)), applied to data from the isotropic simulation I. Recall  $Y_l^\pm = \langle (\ell \cdot \delta z^\mp) |\delta z^\pm|^2 \rangle$ . Different curves represent the results of 36 different lag directions uniformly distributed on a sphere. Each curve represents the average of the  $Y_l^+/\ell$  and  $Y_l^-/\ell$  terms for a fixed lag direction. The dark blue dashed horizontal line (at 0.795) indicates the actual energy dissipation rate. A standard procedure is to assume that the peak values provide estimates of the dissipation rate and the corresponding  $\ell$  values locate in the middle of the inertial range.

included to minimize time-dependent effects while examining residual transient dependence on direction, an effect that will be discussed further below.

The analyses presented here are carried out at the simulation times indicated in Figure 2, which shows the time evolution of the mean-square current density and mean-square vorticity for each run. We can compute the exact value of the dissipation rate,  $\epsilon_{\text{diss}}$ , using Equation (5). Table 1 lists the values of  $\epsilon_{\text{diss}}$  for each simulation at the time our analysis is performed.

In the following sections, we carry out several types of analyses centered around the strategy of employing the third-order structure function to estimate the dissipation rate in the simulation. The exact dissipation rate,  $\epsilon_{\text{diss}}$  from Equation (5), is used to study the accuracy of these various strategies.

#### 4. Results: 1D form Third-order Law

In this section, we apply Equation (10), a simplified and widely used 1D form of the third-order law referred to as Method I, to simulation data obtained from both isotropic (Section 4.1) and anisotropic cases (Section 4.2). We examine the inertial ranges and dissipation rates estimated from this 1D form. We will consider estimates based on individual directions as well as partial averages over directions, but we do not here attempt a full integration over a solid angle, which is a requirement for Method III.

##### 4.1. Isotropic Case

We consider the driven  $B_0=0$  isotropic simulation I. Figure 3 displays the curves for  $(Y_l^+ + Y_l^-)/\ell$  as a function of  $\ell$ , individually computed for each of 36 selected directions uniformly distributed on a sphere. The 3D trilinear interpolation method (Bai & Wang 2010) is used to calculate magnetic and velocity fields not located on grid points. Each curve represents a certain lag direction, and the value along the y-axis is the average of  $-3Y_l^+/(4\ell)$  and  $-3Y_l^-/(4\ell)$ . The peak value of  $-3(Y_l^+ + Y_l^-)/(8\ell)$  is used to estimate the dissipation rate.

We observe that for all the curves the peak values are smaller than the actual dissipation rate,  $\epsilon_{\text{diss}}$ , which is explained in Section 5.2. It is also evident in Figure 3 that the inertial ranges associated with the different lag directions are broadly consistent in extent, with some variation in the peak values. This indicates that at the instant of time of this analysis, even this nominally isotropic simulation admits some degree of variation over directions. It is reasonable to suppose that directional averaging might improve the estimates of dissipation rate in this case; we will take up this discussion in a later section.

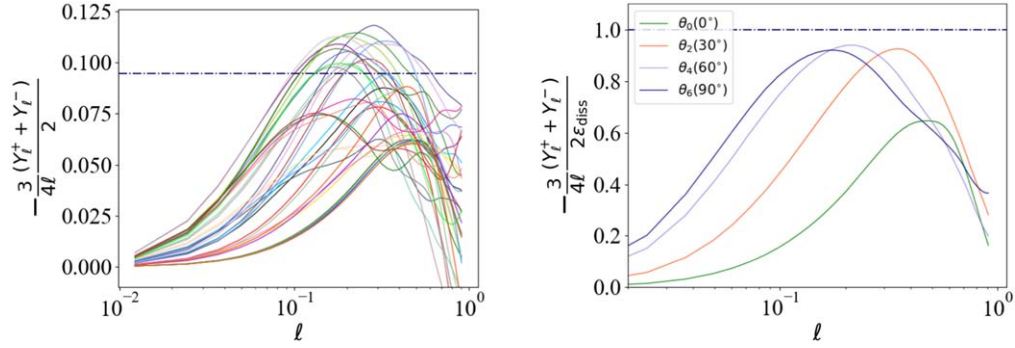
##### 4.2. Anisotropic Case

The anisotropic simulations we consider have a mean magnetic field,  $B_0\hat{z}$ , with  $B_0=1$  or 2 and differing cross helicities (see Table 1). In this section, we only consider the anisotropic simulation III. To examine how the lag direction impacts the Yaglom term in anisotropic MHD, we evaluate the dissipation rate in simulation III using Method I, i.e., the 1D form of the third-order law, Equation (10). Separate estimates are made using lags in each of 36 directions, uniformly spaced in colatitude and azimuthal angles ( $\Delta\theta = \frac{\pi}{6}$  and  $\Delta\phi = \frac{\pi}{3}$ ). The left panel of Figure 4 demonstrates that the peak values associated with these different lag directions occur at different lags. The levels of the maxima also vary, in some cases exceeding the true dissipation rate. Similarly, the *inertial ranges* associated with the different lag directions also vary in bandwidth and position.

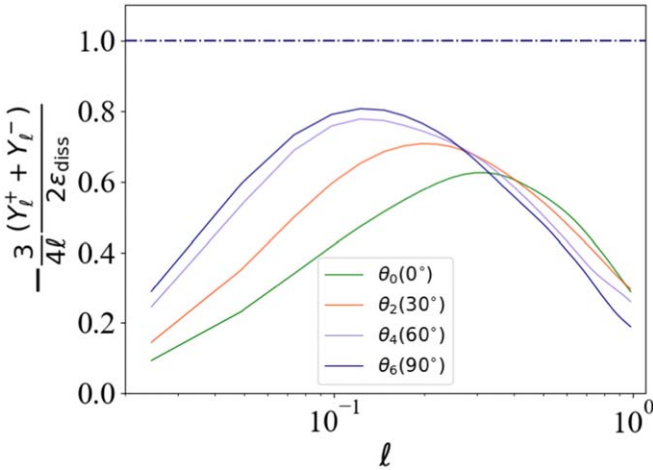
In order to further study the effect of partial averaging in the presence of a global magnetic field, we group the lag directions by their corresponding polar angle  $\theta$ . Recall that the global magnetic field is in the  $+\hat{z}$  direction. For each polar angle, we average the  $Y_l^\pm/\ell$  terms over six azimuthal directions (Figure 4, right panel). We observe that the peak of each curve shifts to smaller lags as  $\theta$  increases. Moreover, the peak value associated with the quasi-parallel case ( $\ell\parallel\mathbf{B}_0$  and  $\theta=0$ ) provides a significantly lower estimate of  $\epsilon_{\text{diss}}$  than do the larger  $\theta$  cases, which have peak values comparable to the actual dissipation rate. This reflects the well-known fact that energy transfer proceeds more rapidly perpendicular to an applied magnetic field (Shebalin et al. 1983).

An analysis similar to that of Figure 4 is shown in Figure 5 for simulation II, which has low  $\sigma_c$  and  $B_0=1$ . Here, once again, larger  $\theta$  values, more strongly perpendicular lag directions, are associated with the inertial range behavior found at smaller lags. It is interesting to examine the degree of anisotropy of the energy transfer by looking at the disparity of the cascade rate estimates at varying angles in the two cases, simulation II with weaker  $B_0$  and smaller  $\sigma_c$ , and simulation III with stronger  $B_0$  and larger  $\sigma_c$ . The ratio of the strongest estimate to the weakest over angles is actually slightly greater in simulation II (ratio  $\sim 1.4$ ) than in simulation III (ratio  $\sim 1.3$ ), even though simulation III has the stronger mean magnetic field. Superficially this result appears to be anomalous; however, the significant contrast in cross helicity ( $\sigma_c$ ) values is a likely explanation, as this is another factor that can influence nonlinear timescales, cascade strength, and anisotropy.





**Figure 4.** A collection of estimates of dissipation rate using Method I, the 1D form third-order law (Equation (10)), applied to data from the high  $\sigma_c$ ,  $B_0 = 2\hat{z}$  anisotropic simulation III. Left: each curve represents the average of the  $Y_l^+/\ell$  and  $Y_l^-/\ell$  terms for a fixed lag direction. The dashed horizontal line indicates the actual energy dissipation rate. Peak values estimate the dissipation rate and (horizontal) location of a peak roughly locates in the middle of the inertial range. Right: same data as the left panel, normalized by  $\epsilon_{\text{diss}}$ , and averaged over azimuthal angle  $\phi$ . Each curve is for a fixed polar angle  $\theta$ , and averaged over six equally spaced azimuthal angles with  $\Delta\phi = \frac{\pi}{3}$ .



**Figure 5.** Evaluating the dissipation rate using the 1D form third-order law (Equation (10), Method I) for the low  $\sigma_c$ ,  $B_0 = 1$  anisotropic simulation II. Curves correspond to lag directions with the indicated polar angle  $\theta$  and averaged over six equally spaced azimuthal angles,  $\phi$ . Each curve represents the average of the corresponding  $Y_l^\pm/\ell$  terms, normalized by the true dissipation rate.

#### 4.3. Comparison between the Isotropic and Anisotropic Cases Using the 1D form

The above Method I results for estimating  $\epsilon_{\text{diss}}$  indicate clear differences between the isotropic and anisotropic situations. In each system, we chose 36 different lag directions, distributed uniformly on a sphere, and employed the 1D form of the third-order law (Equation (10)) to calculate  $(\epsilon^+ + \epsilon^-)/2$  for each direction. For the driven (statistically steady) isotropic simulation we found that the inertial range and also the corresponding energy cascade rate determined this way are roughly independent of the lag directions (Figure 3), as expected for isotropy. For the two anisotropic cases, different lag directions vary much more in terms of the cascade rate estimates as well as location and bandwidths of the suggested inertial range(s). The conclusion is that it is difficult to accurately determine the energy cascade rate of an anisotropic system using the 1D form third-order law (Equation (10)), especially with one or a small number of computed lag directions. For an isotropic system, the situation is somewhat better, although some modest variation in the estimated cascade rate is seen in varying lag directions.

## 5. Results: Full Directional Averaging

Given the variability we have seen in the above numerical experiments in both isotropic and anisotropic cases, we expect to obtain improved results starting from either the divergence (3D) form Equation (9) (Method II), valid within a well-defined inertial range, or from the von Kármán–Howarth equation, Equation (4) or (7), which is broadly applicable even when an inertial range is not present. Another strategy, which we now explore, is to compute the dissipation rates  $\epsilon^\pm$  using Method III, the fully direction-averaged 1D form of the third-order law, Equation (14).<sup>6</sup>

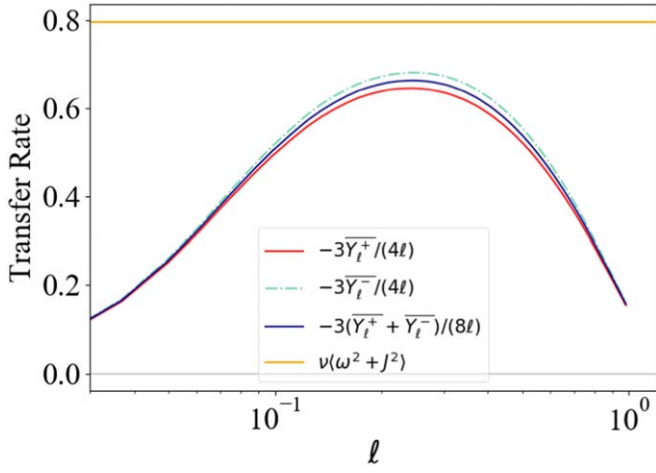
As emphasized above, based on the generalization of the result in Nie & Tanveer (1999) to the MHD von Kármán–Howarth equation, one finds that direction averaging can reduce the problem to the 1D integration over the full  $4\pi$  solid angle, see, for example, Equation (12). We can then consider just the radial component if the chosen lag directions completely cover the sphere (details of equations and discretization method can be found in the Appendix). In particular, when an inertial range is present, the direction-averaged MHD Yaglom law Equation (14) emerges as an exact result.

Here, we proceed numerically, employing a discretization method like Equation (A7) to calculate the direction-averaged 1D form third-order law Equation (14) in the inertial range, and a similar method for the direction-averaged von Kármán–Howarth equation Equation (12) (details in the Appendix). Again, 3D trilinear interpolation is used for values of magnetic field and velocity not located on grid points. In order to get a uniform distribution, at any fixed lag length, we vary the direction of the lag. Let  $\theta$  be the polar angle, and  $\phi$  be the azimuthal angle, in such case, we keep  $\Delta\theta$  and  $\Delta\phi$  to be fixed, which are  $\pi/12$  and  $\pi/6$ , respectively, for simulations with resolution 1024 ( $\pi/8$  and  $\pi/4$  for simulations with resolution 512).

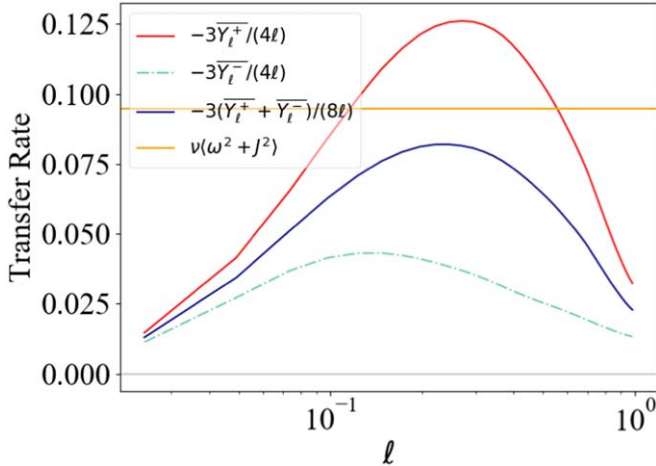
### 5.1. Method III: Direction-averaged 1D Form Third-order Law

In Figures 6 and 7, we show the directional average of 1D form third-order law, with its assumption of a well-defined

<sup>6</sup> We already showed the results in Figure 1 obtained from the von Kármán–Howarth equation (Equation (4) or (7)), which was also direction averaged as in Equation (11). This averaging over directions in Figure 1 was not required but increased the accuracy of the computation.



**Figure 6.** Evaluating dissipation rates for isotropic simulation I using Method III, the direction-averaged 1D form third-order law, Equation (14). Here, the direction-averaged  $Y_\ell^\pm = \langle (\ell \cdot \delta \mathbf{z}^\pm) |\delta \mathbf{z}^\pm|^2 \rangle$  term is designated as  $Y_\ell^\pm$ . The dark blue curve is the average of the two  $Y_\ell^\pm$  terms, and the orange horizontal line indicates the exact dissipation rate.

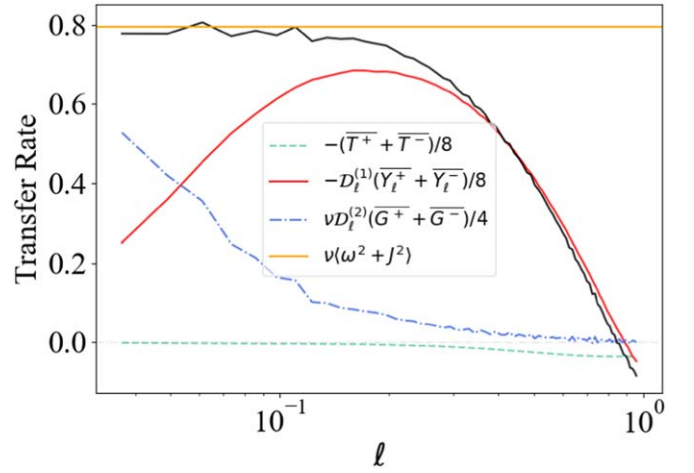


**Figure 7.** Method III, direction-averaged 1D form third-order law (Equation (14)), applied to data from anisotropic simulation III, which has high  $\sigma_c = 0.7$  and  $B_0 = 2$ . The same color code as Figure 6 is used.

inertial range, using data from simulations I and III. Recall that simulation III has a high cross helicity, leading to a large difference between “+” and “−” terms in Figure 7. The dark blue curve is the average of the minus and plus terms. We see that the dissipation rate computed from the direction-averaged 1D form is slightly smaller than the exact dissipation rate in both isotropic and anisotropic cases. This indicates a relatively minor role of the time variation term and the dissipative term in the von Kármán–Howarth equation for both cases.

### 5.2. Direction-averaged von Kármán–Howarth Equation

We now demonstrate the estimation of energy transfer rates using all relevant terms in the direction-averaged von Kármán–Howarth equation Equation (12). Note that in a driven system, the von Kármán–Howarth equation Equation (4) should be extended to include a large-scale forcing term  $\langle \delta \mathbf{z}^\pm \cdot \mathbf{F}_\ell \rangle$  on the right-hand side. The associated direction-averaged form can be



**Figure 8.** Terms of the direction-averaged von Kármán–Howarth equation Equation (12) in the driven isotropic simulation I at  $t = 8$ . The orange horizontal line indicates the actual dissipation rate. The black curve, representing the total transfer rate, is the sum of the three lines representing the  $Y$ ,  $G$ , and  $T$  terms, which contributes to the transfer rate on large scales, as in Equation (15), is not plotted.

written as

$$\overline{T^\pm} + \mathcal{D}_\ell^{(1)} \overline{Y_\ell^\pm} - 2\nu \mathcal{D}_\ell^{(2)} \overline{G^\pm} = -4\epsilon^\pm + \overline{\langle \delta \mathbf{z}^\pm \cdot \mathbf{F}_\ell \rangle}. \quad (15)$$

This analysis is first carried out for simulation I, a driven isotropic system. Figure 8 displays these direction-averaged contributions to the von Kármán–Howarth equation, omitting the forcing term. We see that at small scales the sum of the (direction-averaged) time variation term ( $-\overline{T^\pm}$ ), cascade term ( $-\mathcal{D}_\ell^{(1)} \overline{Y_\ell^\pm}$ ), and dissipative term ( $2\nu \mathcal{D}_\ell^{(2)} \overline{G^\pm}$ ) add up to the actual dissipation rate; evidently, the driving force term does not play a role at these scales. On the other hand, at large scales, the forcing term (not shown) is dominant, and the sum of the other three terms drops as  $\ell$  increases. One may notice that when the Yaglom term  $-\mathcal{D}_\ell^{(1)} (\overline{Y_\ell^+} + \overline{Y_\ell^-})/8$  is at its peak of  $\sim 86\%$  of  $\epsilon_{\text{diss}}$ , the dissipative term  $\nu \mathcal{D}_\ell^{(2)} (\overline{G^+} + \overline{G^-})/4$  is  $\sim 12\%$  of  $\epsilon_{\text{diss}}$ , which is small although not quite negligible. Comparing this to the results shown in Figure 6, obtained using Method III and Equation (14), we see that the direction-averaged 1D form of the Yaglom law, which *assumes* inertial range conditions, actually produces a smaller estimate for the cascade rate, with a peak of  $\sim 83\%$  of  $\epsilon_{\text{diss}}$ .

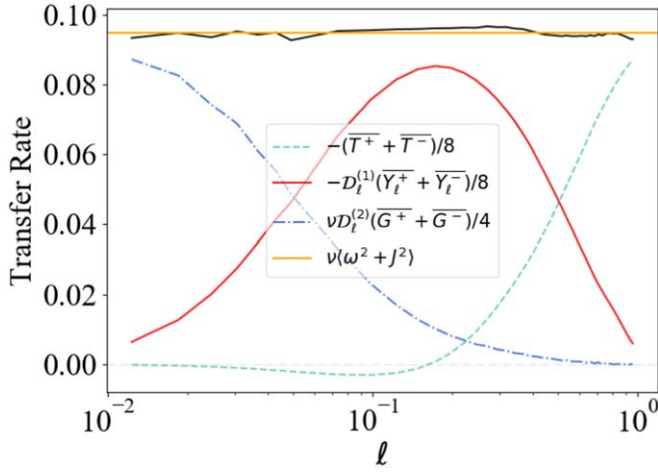
The equivalent results for the decaying anisotropic simulation III with global field  $\mathbf{B}_0 = 2\hat{\mathbf{z}}$  are shown in Figure 9. Energy balance is again evident, in this case at all scales. Furthermore, the peak value of the  $-\mathcal{D}_\ell^{(1)} (\overline{Y_\ell^+} + \overline{Y_\ell^-})/8$  curve is  $\sim 87\%$  of  $\epsilon_{\text{diss}}$ , which is usefully close to the true value.

### 5.3. Comparison between Anisotropic Cases

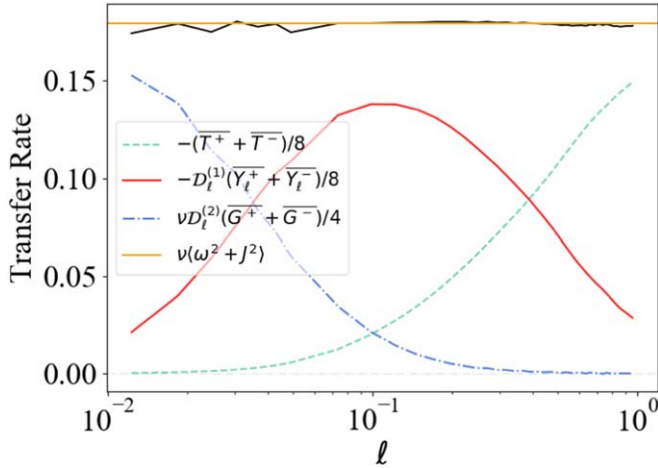
We recall that two anisotropic simulations (Runs II and III) are included, in part, to explore the parameter variations that may influence the results. These simulations have different magnetic field strengths and different levels of cross helicity, both of which are known to influence the nature of the anisotropic cascade (Pouquet et al. 1986; Politano & Pouquet 1998a; Oughton et al. 2015).

In this section, we compare the results from these two anisotropic cases, simulations II and III. First, as a comparison with Figure 9 for simulation III, we show in Figure 10 the terms of the direction-averaged von Kármán–Howarth equation





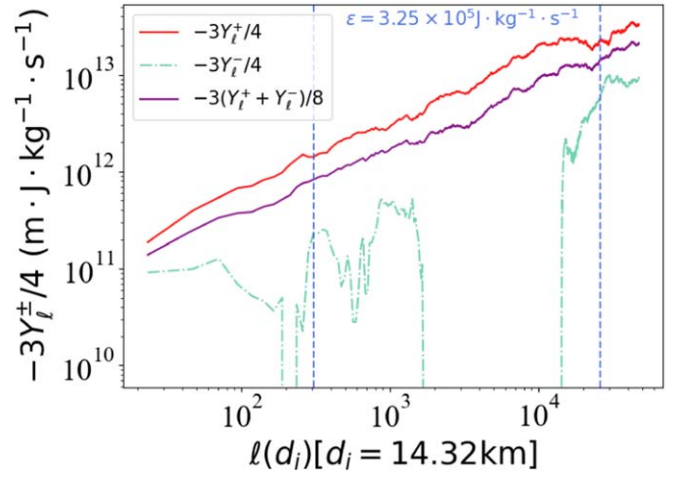
**Figure 9.** Terms in the direction-averaged von Kármán–Howarth equations, same as Figure 8, except using data from anisotropic simulation III ( $B_0 = 2$ , high  $\sigma_c$ ). Energy balance is obtained at all scales, as indicated by the comparison of the actual dissipation rate calculated from  $\nu(\omega^2 + J^2)$  with the black line, which is the sum of the three lines representing the  $Y$ ,  $G$ , and  $T$  terms.



**Figure 10.** Terms in the direction-averaged von Kármán–Howarth equations, same as Figure 9, except using data from anisotropic simulation II ( $B_0 = 1$ , low  $\sigma_c$ ). Energy balance is obtained at all scales.

(Equation (12)) for simulation II, which add up to the exact dissipation rate. However, for simulation II, due to the non-negligible effect of the time variation and dissipative terms, we observe that the peak value of the  $-\mathcal{D}_\ell^{(1)}(\overline{Y}_\ell^+ + \overline{Y}_\ell^-)/8$  curve is much smaller than the exact dissipation rate (approximately 77%). Thus, one can also expect that using the direction-averaged 1D form third-order law (Method III), which only considers the Yaglom term  $\overline{Y}_\ell^\pm$ , will yield a less accurate estimate for the cascade rate.

As discussed in Section 2, large Reynolds numbers are required in order to have an inertial range that is well separated from the dissipation range. Unfortunately, due to limited computing capabilities, this is not the case for our simulations. Furthermore, it has been assumed that the time variation term is negligible in Equation (4), along with the dissipation term. Again, this is not the case for the anisotropic simulations we report on herein (see the discussion of Figures 9 and 10). Since our simulation II is not in a regime where the cascade terms ( $\nabla_\ell \cdot \mathbf{Y}^\pm$ ) dominate over the time variation and dissipation



**Figure 11.** The 1D form third-order law (Method I) is used for PSP observations to estimate the energy dissipation rate (data from 2018 November 3–8, with averaged helio-distance  $37.9 R_\odot$ ; lags are in units of the ion inertial length,  $d_i$ ). The indicated value of  $\epsilon = 3.25 \times 10^3 \text{ J/kg-s}$  is obtained using a least mean squares linear fit to  $3(Y_\ell^+ + Y_\ell^-)/8 = \epsilon \ell$ . The inertial range in which we perform the fit to the 1D form is indicated by the two vertical dashed lines.

terms, the transfer rates estimated using a third-order law are significantly less than the actual dissipation rate, even in lag directions perpendicular to  $\mathbf{B}_0$ , which usually give values closer to the exact energy transfer rate (see Figure 5). Of the runs, we consider that simulation III is perhaps the least limited in this respect. In particular, as Figure 9 indicates, the peak  $-\mathcal{D}_\ell^{(1)}(Y_\ell^+ + Y_\ell^-)/8$  contribution is  $\sim 13\%$  smaller than  $\epsilon_{\text{diss}}$ . However, the situation is complicated since in some parts of the inertial range there is cancellation of the (negative at small  $\ell$ ) time variation term  $-(T^+ + T^-)/8$  and the dissipative term  $\nu \mathcal{D}_\ell^{(2)}(\overline{G}^+ + \overline{G}^-)/4$ .

## 6. Cascade Rate and Single Spacecraft Sampling

Single spacecraft observations in the solar wind provide lags in only one direction, thus we can apply only the 1D form third-order law, usually that written as Equation (10); and described as Method I, see Section 2.1. The same definition  $Y_\ell^\pm = \langle (\hat{\ell} \cdot \delta \mathbf{z}^\mp) |\delta \mathbf{z}^\pm|^2 \rangle$  is employed, but now  $\mathbf{z}^\pm = \mathbf{v} \pm \mathbf{B} / \sqrt{\mu_0 \langle n_i \rangle m_i}$ , where  $\mu_0$  is the magnetic permeability of free space and  $m_i$ ,  $\langle n_i \rangle$  are, respectively, the mass and (interval averaged) number density of the solar wind protons. Here, we analyze measurements made by PSP from 2018 November 3–8; the time cadence of the data is 1 s. The purpose is not to provide an exhaustive treatment of the solar wind cascade rates. Instead, we present an example to inform and support our discussion.

The dissipation rate  $\epsilon_{\text{diss}}$  can be estimated by performing a linear fit in the inertial range, where the corresponding slope gives the value of  $\epsilon_{\text{diss}}$ . We choose the inertial range as the range separated from the correlation length and the estimated scale at which kinetic effects become important. The latter is typically a few ion inertial scales, as indicated in Figure 11. Generally, we also examine the energy spectra (not shown) to ensure that a reasonable power-law distribution is found in the selected range of scales. A linear least mean-square method is employed over the selected inertial range for determining the best-fitting slope to the computed values of  $Y_\ell^\pm$ . Note that Figure 11 is plotted in log–log form, while the best fits are

computed in linear–linear space. One should not be confused with the slope of the line in log–log form and the estimated dissipation rate  $\epsilon$ . Plotted this way (log–log) the slope of the line indicates the power law in lag, which is expected to be linear, while the level of the line determines the estimated dissipation rate.

Third-order statistics are notoriously noisy in the solar wind and a single example will not be fully representative. The sample result shown can be meaningfully compared with other recent third-order analyses, including those that employ PSP data (Bandyopadhyay et al. 2020; Andrés et al. 2021, 2022). However, detailed comparisons are beyond the scope of the current study. Recent studies also indicate the presence of anisotropy in computed correlation scales (Cuesta et al. 2022) as well as anisotropy in the energy spectrum at kinetic scales (Huang et al. 2022; Zhang et al. 2022) in the PSP data sets, which may suggest anisotropy of nonlinear energy transfer. More evidence has been shown in Andrés et al. (2022), which examines variations of third-order law with decomposition into parallel and perpendicular components using PSP data.

As discussed earlier, in anisotropic configurations, the dissipation rate we obtain from the 1D form third-order law Equation (10) depends on the lag direction, as is evident in Figure 4 for simulation III and Figure 5 for simulation II. In addition, the inertial range is also not uniquely determined in anisotropic cases and estimates of the optimal range of lags to associate with a putative inertial range vary with the lag direction as seen in the same figures. Therefore, the estimates of dissipation rate vary when analyzing different directions and assuming different inertial ranges. Nonetheless, the 1D form third-order law may provide reasonable approximations of the actual dissipation rate if the directional variability in values of the estimated dissipation rate is acceptable. For example, cascade rates estimated from different peaks in Figure 4 vary by about 50% of the exact dissipation rate.

The solar wind has a global magnetic field, and in the inner heliosphere, a relatively high cross helicity. These features are similar to those of simulation III. Examining the results of our analysis for this run (Figure 4, right panel), the error in the estimates of the cascade rate obtained from the 1D form third-order law can usually be assessed from the variation in the peak value and the variation in the location of the peak in the lag axis.

## 7. Discussion and Conclusions

We have examined the properties of several formulations for analyzing energy transfer in homogeneous MHD turbulence. The von Kármán–Howarth equations in increment form, Equation (4), symbolically written as Equation (7), provide the most complete treatment. These are exact equations and account for dissipation, time dependence, nonlinear transfer, and anisotropy. Quantitative evaluation of the several terms in the von Kármán–Howarth equations affords direct insight into the conditions required to identify a range of scales that can reasonably be viewed as an *inertial range*. Ideally, in such a range, Kolmogorov’s assumptions of steady dissipation-free transfer across scales can be realized, and the only term that makes a substantial contribution is the one involving the third-order structure functions,  $Y^\pm$ . In that case, various forms of the Kolmogorov–Yaglom (Frisch 1995) law become relevant, and specifically in MHD, the third-order law derived first by Politano & Pouquet (1998b).

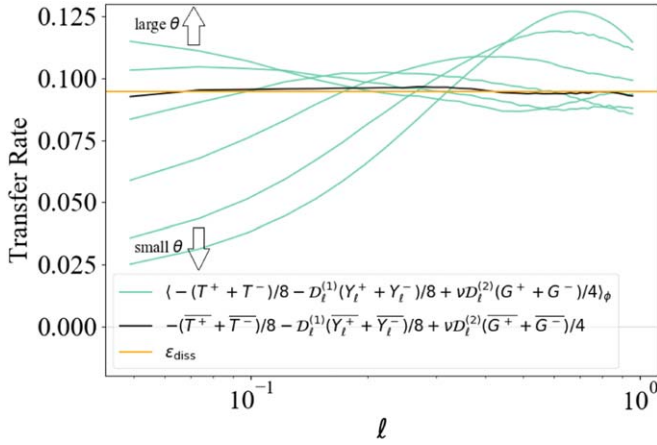
When less information is available, and in particular when it is impractical to determine three-dimensional derivatives in lag space, researchers have traditionally adopted one of several approaches to simplify the estimation of the transfer rate, which in steady conditions is the cascade (or dissipation) rate. We have examined several issues that affect these familiar approximations.

In our study, we examined both the von Kármán–Howarth equation and a simpler form of the third-order law for incompressible MHD simulations of turbulence systems. In MHD under different global magnetic field conditions, one can compute the correct value for the cascade rate if each term of the von Kármán–Howarth equation, Equation (4) or (7), can be computed exactly. With a numerical discretization, only approximate values can be obtained. Nevertheless, averaging the von Kármán–Howarth equation in a sufficient number of independent directions (e.g., spanning a spherical surface), and keeping only the radial ( $\hat{\ell}$ ) components of the so-obtained  $Y^\pm$ , can provide accurate results. This strategy is based on a rigorous reduction of the problem to a one-dimensional direction-averaged form, a direct extension to MHD of the hydrodynamic result (Nie & Tanveer 1999). The direction-averaging approach may be particularly useful when adapted for use with multi-spacecraft data sets (for which there are typically only a small number of lag directions available) to estimate local cascade rates for space plasma turbulence. The accuracy of this method for different simulations is reported in Section 5 and displayed in Figures 8–10.

For further simplification, we require the existence of an inertial range of substantial length (i.e., a very high Reynolds number) to justify the use of what we have called the third-order laws (Section 2.1.1). Since the condition of infinite Reynolds number cannot be achieved, we are not able to observe a perfect inertial range, thereby leading to discrepancies between the actual cascade rate and the one determined from the third-order term. An advantage of these simplified forms is that they ignore dissipative and time variation effects, which are difficult to measure experimentally. The 3D form of the third-order law requires that at least some measurements are available in different directions and provides a reasonable estimate of 3D derivatives in lag space in simulations (Verdini et al. 2015). In the presence of time stationarity, the 3D form third-order law can provide an accurate estimate of the energy transfer rate in the inertial range.

The further assumption of isotropy is often used for in situ measurements of solar wind turbulence (e.g., Stawarz et al. 2009; Osman et al. 2011) and magnetic reconnection in Earth’s magnetosheath (e.g., Bandyopadhyay et al. 2020). In the presence of isotropy, the 3D form third-order law can be simplified to a 1D form, which employs only one lag direction. For isotropic MHD simulations, the 1D form third-order law provides a reasonable approximation, with some statistical variation with changing lag direction.

Issues regarding the accuracy of energy transfer rate estimation become still more significant when anisotropy is induced by a mean magnetic field, a circumstance expected to be of significance in space and astrophysical plasmas. We report on two anisotropic simulations (Figures 4 and 5) in Section 4.3 and (Figures 9 and 10) in Section 5.3. From these results, it is apparent that error in estimation from the 1D form third-order law follows from a combination of effects due to the magnitude of the global magnetic field (anisotropy), the



**Figure 12.** Two types of angular averaging of the von Kármán–Howarth equation Equation (8) applied to data from the  $B_0 = 2$ , high  $\sigma_c$  simulation III. Terms with an overbar indicate an average over a full  $4\pi$  solid angle (all lag directions distributed uniformly on a sphere); see Equation (12). Each green curve is calculated for a different fixed polar angle  $\theta$  averaged over 12 azimuthal angles  $\phi$ , with the averaging denoted by  $\langle \dots \rangle_\phi$ . The black curve is the averaged value of all the green curves after weighting by  $\sin \theta$ .

contribution of the dissipative term, and a lack of time stationarity. These errors can add up to be  $\sim 50\%$  of the exact dissipation rate in our simulations. We conclude that the (unaveraged) 1D form provides a correct order of magnitude result for the moderate levels of anisotropy found in the parameters we adopted.

Several aspects of the effects of anisotropy are summarized in Figure 12, which includes an assessment of the direction-averaged von Kármán–Howarth equation Equation (12). We intend to highlight variations of energy transfer for different polar angles  $\theta$ , and therefore we do not show variations with varying azimuthal angle  $\phi$ . In Figure 12, we plot (green curves) the sum of the time variation  $-(T^+ + T^-)/8$ , the 1D Yaglom term  $-\mathcal{D}_\ell^{(1)}(Y_\ell^+ + Y_\ell^-)/8$ , and the 1D dissipative term  $(\nu \mathcal{D}_\ell^{(2)}(G^+ + G^-)/4)$ , each averaged over 12 azimuthal angles for fixed polar angles ranging over the interval  $0 \leq \theta \leq 90^\circ$ . Recall the definitions of the 1D operators  $\mathcal{D}^{(1)}$  and  $\mathcal{D}^{(2)}$  are given below Equation (12). The average over  $\phi$  is indicated by  $\langle \dots \rangle_\phi$  in the legend. Note that the procedure is not equivalent to full  $4\pi$  solid angle averaging, which is indicated by an overbar as in Equation (12). Clearly averaging over  $\phi$  is only a partial averaging and, in general, falls short of the effect of fully directional averaging.

The average of the contributions from each  $\theta$  can be weighted by  $\sin \theta$  and summed, to provide an approximation to a proper average over the sphere, which is the full  $4\pi$  solid angle averaging indicated by the overbar as in Equation (12). This sum is also shown in Figure 12 (as the black line). We observe that this summation closely adds up to the exact dissipation rate, also shown (orange line). This demonstrates the approximate convergence that is expected based on the MHD generalization of the Nie & Tanveer (1999) exact result for hydrodynamics, as we discussed in previous sections.

To delve somewhat further into this analysis of anisotropy, we note that since each partially averaged (green) curve in Figure 12 is obtained at one only polar angle  $\theta$  relative to the mean field, we see a large variance in the sum of the three (LHS) terms in the von Kármán–Howarth equation. At small scales, the top curve, having the largest estimated total transfer

rate, corresponds to  $\theta(\ell, \mathbf{B}_0)$  close to  $90^\circ$  and the bottom curve, with the lowest estimated transfer rate, corresponds to  $\theta(\ell, \mathbf{B}_0)$  near  $0^\circ$ , almost parallel to the mean field. In fact, the estimated transfer rate at small scales increases monotonically as we increase the polar angle (from  $0^\circ$ – $90^\circ$ ). On the contrary, at large scales, the sum of the three terms is larger for smaller  $\theta$ . As a consequence, the peaks of these curves shift from large scales to small scales as we increase  $\theta$ . In addition, we may notice that these curves are intertwined in the middle range of lags, which is approximately the inertial range (see Figure 9). There is actually a rather narrow range of lags near  $\ell = 0.3$  in which the estimates derived from different polar angles are close to one another, varying by only about  $\pm 10\%$ . Overall, the observed variability at different values of polar angle  $\theta$  emphasizes the necessity of a uniform angular coverage of the lag directions to compute an accurate energy transfer rate in anisotropic cases. It is also consistent with the variability associated with the  $Y_\ell^\pm/\ell$  term (i.e., Method I) that was demonstrated for the anisotropic cases (Figures 4 and 5), and to a lesser extent even for the isotropic case (Figure 3).

This paper has been developed with two main intentions. First we intended to summarize pertinent analytical results relating to the measurement of energy transfer rates beginning with the von Kármán–Howarth equations and leading to several reductions that are essentially third-order (Yaglom) laws, or for MHD, Politano–Pouquet third-order laws. The reduction to Yaglom laws becomes applicable when an inertial range is present, so that all terms but the Yaglom flux become negligible in contributing to the total energy balance over a range of lags in the inertial range. The second purpose has been to provide examples and caveats concerning the use of these methods by application to several moderate-resolution MHD turbulence simulations.

The results are generally seen to be encouraging. Even with significant variation in estimates expected due to variation of lag direction in anisotropic cases, and due to pollution of the putative inertial range by time-dependent and dissipative effects, estimates can be broadly accurate within tolerances of  $\sim 50\%$ . Simulations can generally do better than this, but for single spacecraft observations this may be an acceptable estimate. It is clear that estimates will improve when three-dimensional derivatives in lag space are available, and when a large number of baseline directions are available so one might approach optimal direction averaging. Some progress has been realized along these lines by exploiting these features in the four spacecraft Cluster mission (Osman et al. 2011). Significant advances in evaluating inertial range transfer rates will become available in the Helioswarm mission, comprising nine spacecraft and is currently under development (Klein et al. 2019; Matthaeus et al. 2019; Spence 2019) and a larger 24 point configuration envisioned in the MagneToRE approach (Maruca et al. 2021).

Finally, we mention some limitations of the present study. We have not attempted any examination of the accuracy of third-order laws in differing interplanetary conditions and therefore have shown only a single case of solar wind cascade rate analysis. A complete study of solar wind situations would inevitably require examining variations of a number of interplanetary parameters including fluctuation and mean field strength, wind speed, cross helicity, turbulence age, etc. Such an effort is highly worthwhile, and the present study provides some guidelines regarding how such a major study might be



undertaken, but for brevity and focus, we defer attempts at a comprehensive comparison with varying solar wind conditions to future research.

The present study is also limited to incompressible and simple MHD cases. Including compressibility, Hall effects, and additional physical influences on energy transfer introduces considerable additional complexity to the estimation of the inertial range transfer rate, and requires much more extensive discussion. Some relevant observational results include some of these more general physical descriptions. For example, recent studies employing PSP, MAVEN, Cluster, Magnetosphere Multiscale, and THEMIS data (Banerjee et al. 2016; Hadid et al. 2017, 2018; Andrés et al. 2019, 2021) found moderate increases in compressible energy transfer rate with respect to the incompressible transfer rate. These results point the way to future studies that would generalize the simpler case that we have examined here.

This research was supported in part by the NASA Parker Solar Probe Mission under a GI grant 80NSSC21K1765 and the ISOIS team (Princeton SUB0000165), IMAP project (Princeton SUB0000317), MMS mission under a Theory and Modeling grant 80NSSC19K0565, NASA HSR grants 80NSSC18K1648 and 80NSSC19K0284, and the US National Science Foundation NSFDOE program under grant PHY2108834.

## Appendix

### Reduction of 3D to 1D Forms by Directional Averaging

Starting from Equation (4), let us integrate it over a spherical surface (i.e., over a solid angle), using spherical polar coordinates with  $\ell$  the *radius*. See Nie & Tanveer (1999) and Taylor et al. (2003) for the closely related hydrodynamic case. As in Equation (7), we adopt abbreviations:  $\frac{\partial}{\partial t} \langle (\delta z^\pm)^2 \rangle = T^\pm$ ,  $\langle \delta z^\mp | \delta z^\pm |^2 \rangle = Y^\pm$ ,  $\langle (\delta z^\pm)^2 \rangle = G^\pm$ .

The  $Y^\pm$  term of Equation (7) becomes

$$\begin{aligned} \int_S \nabla_\ell \cdot Y^\pm d\Omega &= \int_0^\pi \int_0^{2\pi} \\ &\times \left[ \frac{1}{\ell^2} \frac{\partial}{\partial \ell} (\ell^2 Y_\ell^\pm) + \frac{1}{\ell \sin \theta} \frac{\partial}{\partial \theta} \right. \\ &\times \left. (\sin \theta Y_\theta^\pm) + \frac{1}{\ell \sin \theta} \frac{\partial}{\partial \phi} Y_\phi^\pm \right] \sin \theta d\phi d\theta \\ &= \int_0^\pi \int_0^{2\pi} \frac{1}{\ell^2} \frac{\partial}{\partial \ell} (\ell^2 Y_\ell^\pm) \sin \theta d\phi d\theta \\ &+ \int_0^{2\pi} \frac{1}{\ell} (\sin \theta Y_\theta^\pm) \Big|_0^\pi d\phi + \int_0^\pi \frac{1}{\ell} (Y_\phi^\pm) \Big|_0^{2\pi} d\theta. \quad (\text{A1}) \end{aligned}$$

By periodicity, the integrals of the  $\theta$  and  $\phi$  components vanish and therefore

$$\int_S \nabla_\ell \cdot Y^\pm d\Omega = \int_0^\pi \int_0^{2\pi} \frac{1}{\ell^2} \frac{\partial}{\partial \ell} (\ell^2 Y_\ell^\pm) \sin \theta d\phi d\theta. \quad (\text{A2})$$

Similarly, writing the Laplacian of  $G^\pm$  term in spherical polar coordinates also, and then integrating it over a spherical

surface,

$$\begin{aligned} \int_S 2\nu \nabla_\ell^2 G^\pm d\Omega &= \int_0^\pi \int_0^{2\pi} \frac{2\nu}{\ell^2} \\ &\times \left[ \frac{\partial}{\partial \ell} \left( \ell^2 \frac{\partial G^\pm}{\partial \ell} \right) + \frac{1}{\sin \theta} \frac{\partial}{\partial \theta} \left( \sin \theta \frac{\partial G^\pm}{\partial \theta} \right) \right. \\ &+ \left. \frac{1}{\sin^2 \theta} \frac{\partial^2 G^\pm}{\partial \phi^2} \right] \sin \theta d\phi d\theta \\ &= \int_0^\pi \int_0^{2\pi} \frac{2\nu}{\ell^2} \frac{\partial}{\partial \ell} \left( \ell^2 \frac{\partial G^\pm}{\partial \ell} \right) \sin \theta d\phi d\theta, \quad (\text{A3}) \end{aligned}$$

where the  $\partial_\theta$  and  $\partial_\phi$  dependent terms also vanish after integration; in a numerical (discretized) evaluation this vanishing relies on a proper distribution of lag directions.

Using these results we can write the integral of Equation (7) over a solid angle as

$$\begin{aligned} \int_0^\pi \int_0^{2\pi} T^\pm \sin \theta d\phi d\theta + \int_0^\pi \int_0^{2\pi} \\ \times \frac{1}{\ell^2} \frac{\partial}{\partial \ell} (\ell^2 Y_\ell^\pm) \sin \theta d\phi d\theta \\ - \int_0^\pi \int_0^{2\pi} \frac{2\nu}{\ell^2} \frac{\partial}{\partial \ell} \left( \ell^2 \frac{\partial G^\pm}{\partial \ell} \right) \sin \theta d\phi d\theta = -16\pi \epsilon^\pm, \quad (\text{A4}) \end{aligned}$$

where  $4\epsilon^\pm \int_0^\pi \int_0^{2\pi} \sin \theta d\phi d\theta = 16\pi \epsilon^\pm$  provides the last term. Abbreviating the average over a full  $4\pi$  solid angle by an overbar, this equation leads immediately to Equation (12).

When analyzing simulation data, these integrals are evaluated using discrete approximations. To illustrate this we consider the simpler well-defined inertial range case, the 3D form of the third-order law, Equation (9), integrated over a solid angle. Using Equation (A2) in Equation (9), multiplying by  $\ell^2$ , and integrating over both  $d\Omega$  and  $\ell$  yields

$$\int_0^\pi \int_0^{2\pi} Y_\ell^\pm \sin \theta d\phi d\theta = -\frac{4}{3} \epsilon^\pm \int_0^\pi \int_0^{2\pi} \sin \theta d\phi d\theta. \quad (\text{A5})$$

If the average over full  $4\pi$  solid angle is again denoted by an overbar, this result states that


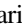


$$\overline{Y_\ell^\pm} = \overline{\langle \hat{\ell} \cdot \delta z^\mp | \delta z^\pm |^2 \rangle} = -\frac{4}{3} \epsilon^\pm \ell. \quad (\text{A6})$$





This is written as Equation (14) in the main text. With a simple discretization of  $\theta$  and  $\phi$ , this becomes

$$-\frac{3 \sum_i \sum_j Y_\ell^\pm(\theta_i, \phi_j) \sin \theta_i \Delta \theta_i \Delta \phi_j}{4 \cdot 4\pi} = \epsilon^\pm \ell. \quad (\text{A7})$$

Similar discretization approaches are applied to the more general case, the direction-averaged von Kármán–Howarth equation, Equation (12) or (A4).

### ORCID iDs

Rohit Chhiber  <https://orcid.org/0000-0002-7174-6948>  
 Subash Adhikari  <https://orcid.org/0000-0003-2160-7066>  
 Yan Yang  <https://orcid.org/0000-0003-2965-7906>  
 Riddhi Bandyopadhyay  <https://orcid.org/0000-0002-6962-0959>

Michael A. Shay  <https://orcid.org/0000-0003-1861-4767>  
 Sean Oughton  <https://orcid.org/0000-0002-2814-7288>  
 William H. Matthaeus  <https://orcid.org/0000-0001-7224-6024>  
 Manuel E. Cuesta  <https://orcid.org/0000-0002-7341-2992>

## References

- Adhikari, S., Parashar, T. N., Shay, M. A., et al. 2021, *PhRvE*, **104**, 065206  
 Andrés, N., Sahraoui, F., Galtier, S., et al. 2019, *PhRvL*, **123**, 245101  
 Andrés, N., Sahraoui, F., Hadid, L., et al. 2021, *ApJ*, **919**, 19  
 Andrés, N., Sahraoui, F., Huang, S., Hadid, L., & Galtier, S. 2022, *A&A*, **661**, A116  
 Antonia, R. A., & Burattini, P. 2006, *JFM*, **550**, 175  
 Bai, Y., & Wang, D. 2010, *IEEE Trans. Fuzzy Syst.*, **18**, 1016  
 Bandyopadhyay, R., Chasapis, A., Gershman, D. J., et al. 2020, *MNRAS*, **500**, L6  
 Bandyopadhyay, R., Goldstein, M. L., Maruca, B. A., et al. 2020, *ApJS*, **246**, 48  
 Banerjee, S., Hadid, L. Z., Sahraoui, F., & Galtier, S. 2016, *ApJL*, **829**, L27  
 Biskamp, D. 2003, *Magnetohydrodynamic Turbulence* (Cambridge: Cambridge Univ. Press)  
 Chasapis, A., Matthaeus, W. H., Bandyopadhyay, R., et al. 2020, *ApJ*, **903**, 127  
 Coburn, J. T., Forman, M. A., Smith, C. W., Vasquez, B. J., & Stawarz, J. E. 2015, *RSPTA*, **373**, 20140150  
 Cuesta, M. E., Chhiber, R., Roy, S., et al. 2022, *ApJL*, **932**, L11  
 Dudok de Wit, T. 2004, *PhRvE*, **70**, 055302  
 Elsasser, W. M. 1950, *PhRv*, **79**, 183  
 Frisch, U. 1995, *Turbulence* (Cambridge: Cambridge Univ. Press)  
 Hadid, L., Sahraoui, F., & Galtier, S. 2017, *ApJ*, **838**, 9  
 Hadid, L. Z., Sahraoui, F., Galtier, S., & Huang, S. Y. 2018, *PhRvL*, **120**, 055102  
 Hellinger, P., Verdini, A., Landi, S., Franci, L., & Matteini, L. 2018, *ApJL*, **857**, L19  
 Huang, S., Xu, S., Zhang, J., et al. 2022, *ApJL*, **929**, L6  
 Jokipii, J. R. 1971, *RvGSP*, **9**, 27  
 Kiyani, K. H., Osman, K. T., & Chapman, S. C. 2015, *RSPTA*, **373**, 20140155  
 Klein, K. G., Alexandrova, O., Bookbinder, J., et al. 2019, arXiv:1903.05740  
 Kolmogorov, A. N. 1941a, DoSSR, **30**, 301  
 Kolmogorov, A. N. 1941b, DoSSR, **32**, 16  
 MacBride, B. T., Forman, M. A., & Smith, C. W. 2005, in Proc. Solar Wind 11/SOHO 16, Connecting Sun and Heliosphere, ed. B. Fleck, T. H. Zurbuchen, & H. Lacoste (Noordwijk: ESA), 613  
 MacBride, B. T., Smith, C. W., & Forman, M. A. 2008, *ApJ*, **679**, 1644  
 Maruca, B. A., Agudelo Rueda, J. A., Bandyopadhyay, R., et al. 2021, *FrASS*, **8**, 108  
 Matthaeus, W. H., Bandyopadhyay, R., Brown, M. R., et al. 2019, arXiv:1903.06890  
 McComb, W. D. 1990, *The Physics of Fluid Turbulence* (New York: Oxford Univ. Press)  
 Nie, Q., & Tanveer, S. 1999, *RSPSA*, **455**, 1615  
 Orszag, S. A., & Patterson, G. S. 1972, *PhRvL*, **28**, 76  
 Osman, K. T., Wan, M., Matthaeus, W. H., Weygand, J. M., & Dasso, S. 2011, *PhRvL*, **107**, 165001  
 Oughton, S., & Matthaeus, W. H. 2020, *ApJ*, **897**, 37  
 Oughton, S., Matthaeus, W. H., Wan, M., & Osman, K. T. 2015, *RSPTA*, **373**, 20140152  
 Podesta, J. J., Forman, M. A., Smith, C. W., et al. 2009, *NPGeo*, **16**, 99  
 Politano, H., & Pouquet, A. 1998a, *PhRvE*, **57**, R21  
 Politano, H., & Pouquet, A. 1998b, *GeoRL*, **25**, 273  
 Pouquet, A., Meneguzzi, M., & Frisch, U. 1986, *PhRvA*, **33**, 4266  
 Roy, S., Chhiber, R., Dasso, S., Ruiz, M. E., & Matthaeus, W. H. 2021, *ApJL*, **919**, L27  
 Shebalin, J. V., Matthaeus, W. H., & Montgomery, D. 1983, *JPIPh*, **29**, 525  
 Sorriso-Valvo, L., Marino, R., Carbone, V., et al. 2007, *PhRvL*, **99**, 115001  
 Spence, H. E. 2019, AGUFM, **2019**, SH11B-04  
 Stawarz, J. E., Smith, C. W., Vasquez, B. J., Forman, M. A., & MacBride, B. T. 2009, *ApJ*, **697**, 1119  
 Taylor, M. A., Kurien, S., & Eyink, G. L. 2003, *PhRvE*, **68**, 026310  
 Vasquez, B. J., Smith, C. W., Hamilton, K., MacBride, B. T., & Leamon, R. J. 2007, *JGRA*, **112**, A07101  
 Verdini, A., Grappin, R., Hellinger, P., Landi, S., & Müller, W. C. 2015, *ApJ*, **804**, 119  
 Yang, Y., Matthaeus, W. H., Roy, S., et al. 2022, *ApJ*, **929**, 142  
 Zhang, J., Huang, S., He, J., et al. 2022, *ApJL*, **924**, L21